Geometric Effects Position Renal Vesicles During Kidney Development

Malte Mederacke[1,2,†], Lisa Conrad[1,2,†], Roman Vetter[1,2], and Dagmar Iber[1,2,*]

[1] *Department of Biosystems Science and Engineering, ETH Zürich, Mattenstrasse 26, 4058 Basel, Switzerland*
[2] *Swiss Institute of Bioinformatics, Mattenstrasse 26, 4058 Basel, Switzerland*
[†] *equal contribution*
[*] *corresponding author: dagmar.iber@bsse.ethz.ch*

August 30, 2022

During kidney development, reciprocal signalling between the epithelium and the mesenchyme coordinates nephrogenesis with branching morphogenesis of the collecting ducts. The mechanism that positions the renal vesicles, and thus the nephrons, relative to the branching ureteric buds has remained elusive. By combining computational modelling and experiments, we show that geometric effects concentrate the key regulator, WNT9b, at the junctions between parent and daughter branches where renal vesicles emerge, despite its uniform expression in the ureteric epithelium. This curvature effect might be a general paradigm to create non-uniform signalling in development.

Keywords: renal vesicle, nephron, ureteric bud, kidney development, curvature, cell aggregation, reaction-diffusion model

Introduction

Developmental processes must be coordinated in space and time to form a functional organ. In the kidney, the nephrons and the collecting ducts develop from different parts of the intermediate mesoderm [8]. Yet, the processes are coordinated such that each nephron connects to a different branch element of the ureteric tree — a design that ensures efficient drainage of the collected fluid. While the key molecular regulators of branching morphogenesis and nephrogenesis have been defined [8, 14], the mechanism that positions the nephrons relative to the ureteric tree has remained elusive. Nephrons develop from renal vesicles (RV), which in turn emerge from the epithelisation of mesenchymal cell condensations, so-called pretubular aggregates (PTA) [22]. The PTA/RV form in the corners between parent branches and newly emerging daughter branches during kidney branching morphogenesis (Fig. 1A).

WNT9b is the most upstream regulator of nephrogenesis that has hitherto been identified, and in its absence, no PTA/RV are observed [3]. *Wnt9b* is expressed uniformly in the ureteric epithelium, and WNT9b diffuses to the adjacent metanephric mesenchyme, where it enables the expression of key PTA markers, including *Wnt4* and *Fgf8* [3, 29]. WNT4 is necessary for PTA formation [37], and by itself sufficient to trigger a mesenchymal-to-epithelial transition and subsequent tubulogenesis, although other members of the WNT family (WNT1, WNT3a, WNT7a, WNT7b, but not WNT11) can substitute for WNT4 [17]. WNT4 and the fibroblast growth factor FGF8 engage in a positive feedback by supporting each other's expression, but FGF8 supports RV formation also independent of WNT4 [30, 33]. WNT9b induces RV formation by counteracting the transcription factor SIX2, which supports its own expression, and prevents the differentiation of nephron progenitor cells (NPC) by repressing PTA markers such as *Wnt4* and *Fgf8* [29]. In the absence of *Six2*, ectopic renal vesicles form on the dorsal (cortical) side of the ureteric bud (UB), and the NPC pool depletes rapidly, terminating nephrogenesis after induction of only a few nephrons [32]. Likewise, uniform activation of WNT signalling in the cap mesenchyme (CM) by *Six2-Cre*-driven expression of stabilised β-catenin or by co-culture with glycogen synthase kinase (GSK) inhibitors results in the uniform emergence of ectopic PTA [16, 18, 28]. WNT9b induces nephrogenesis also in isolated metanephric mesenchyme [3], but *Six2-Cre*-driven expression of *Wnt9b* does not result in ectopic RV [16].

Many other signalling factors impact on the WNT9b/WNT4/SIX2 core network. Most prominently, BMP7 and various FGFs support *Six2* and *Cited1* expression and thereby block PTA formation [10, 38]. While BMP7 signalling via the mitogen-activated protein kinase pathway maintains progenitors, SMAD-mediated BMP7 signalling primes progenitors for WNT/β-catenin mediated differentiation [1, 2].

Cell tracking revealed that NPCs move largely stochastically in the CM, and cells that initiate *Wnt4* expression can still return to the *Six2*-positive progenitor pool [6, 19, 21]. There is thus no obvious barrier within the metanephric mesenchyme that would limit cells to RV formation. Given the uniform expression of *Wnt9b* in the ureteric epithelium, the absence of ectopic RV upon *Wnt9b* expression in the CM, and the stochastic, unrestricted movement of CM cells, it has remained unclear why PTA markers emerge only at the junction of parent and daughter branches. We now combine computational modelling and experiments to show that geometric effects result in higher WNT9b concentration levels in the corner niches between parent and daughter branches, where RV form. We further show that a local increase in WNT9b induces ectopic RV. Branching morphogenesis and nephrogenesis thus become spatially coordinated via geometric effects on biochemical signalling.

Results & Discussion

Geometric effects position nephrons in developing kidneys

We reasoned that uniformly secreted WNT9b may become concentrated in the corner niches between parent and daughter branches because of geometric effects, and sought to test this idea with embryonic kidney geometries. Using light-sheet microscopy, we obtained the 3D geometry of a developing kidney at embryonic day (E) 12.5, and segmented the UB (green), the outer border of the stroma, the SIX2-positive CM (orange), and the outlines of the PTA and RV (yellow) (Fig. 1B, Supp Video

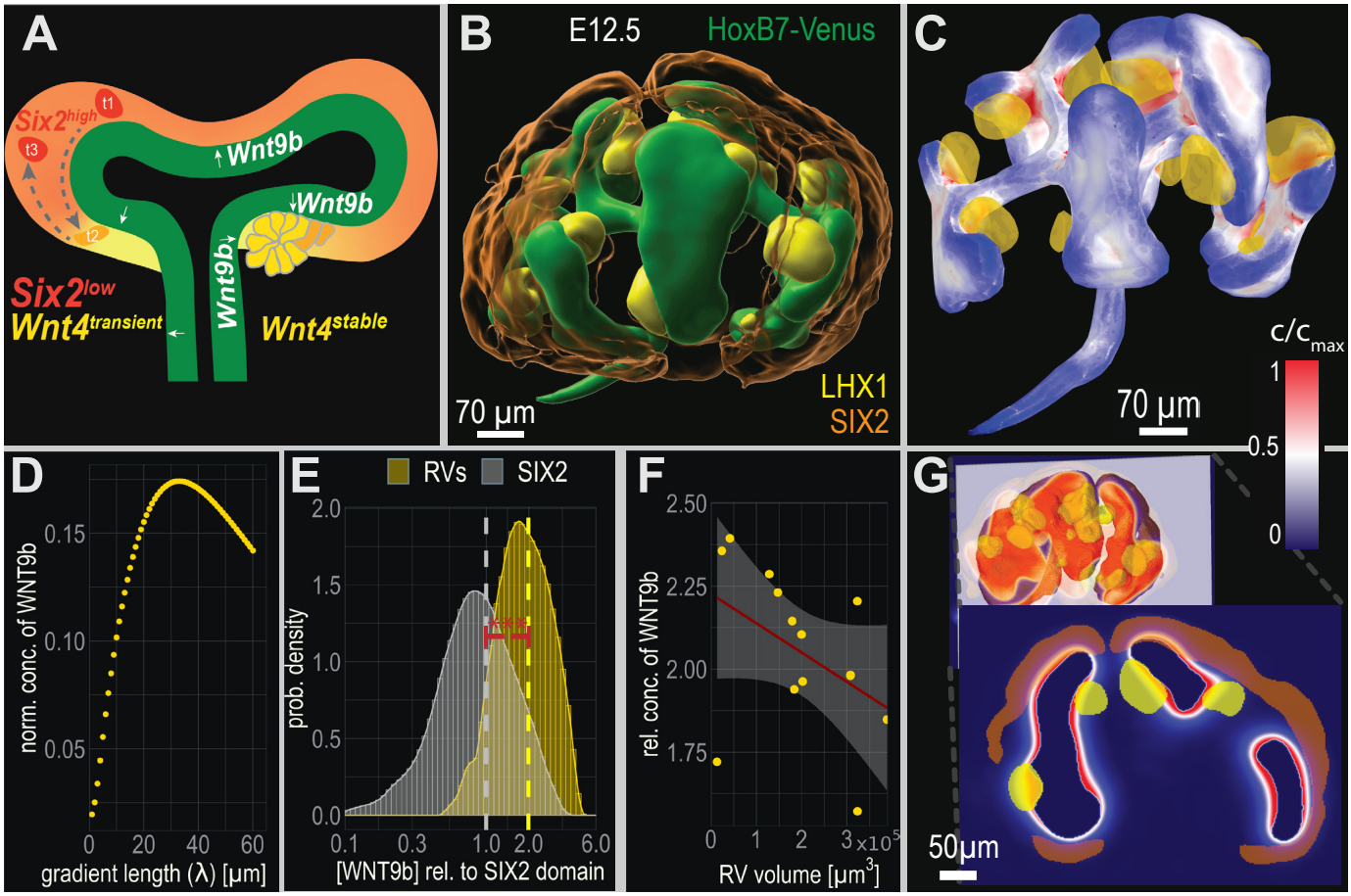

Figure 1: Geometric effects position RV in developing kidneys. (A) Regulation of RV formation. For details, see text. (B) Volumetric light sheet microscopy data of an E12.5 embryonic kidney with surface segmentations for the RV (LHX1, yellow), the UB (HoxB7, green) and the CM (SIX2, orange). (C) 3D simulation of the normalised WNT9b concentration profile with $\lambda = 30$ µm. Uniform secretion of WNT9b from the UB leads to highest ligand concentration (red) in the UB corner regions, coinciding with the position of RVs (yellow). The plot shows integrated concentration profile along the normal direction towards the mesenchyme projected back on the surface of the UB. (D) The highest ligand upconcentration in RVs is achieved for $\lambda \approx 30$ µm. The normalised WNT9b concentration is calculated as the difference between the mean concentration inside the RVs, $\bar{c}_{\mathrm{RV}}$ and the mean concentration inside the SIX2 population, $\bar{c}_{\mathrm{SIX2}}$, relative to the highest concentration inside the kidney, $c_{\max}$: $c_{\mathrm{norm}} = (\bar{c}_{\mathrm{RV}} - \bar{c}_{\mathrm{SIX2}})/c_{\max}$. (E) Relative simulated WNT9b concentration inside the RVs (yellow) and in the SIX2 population (gray). The predicted mean concentration in RVs (yellow dashed line; $c/\bar{c}_{\mathrm{SIX2}} = 1.99 \pm 0.84$ (SD)) is above the predicted mean concentration in the SIX2 population (grey dashed line; $c/\bar{c}_{\mathrm{SIX2}} = 1.00 \pm 0.62$ (SD)) ($p < 0.001$, Welch's two-sample t-test). (F) The predicted WNT9b concentration inside the RVs relative to the SIX2 population is higher in smaller RVs. The red line and gray shade represent a linear fit with its standard error ($R^2 = 0.2$). (G) A cross-section highlighting the relative location of the CM (orange), RVs (yellow), and the simulated concentration gradient (blue-red colormap).

S1). The PTA and RV, as marked by LHX1 (yellow) [25], form in the corners between parent and daughter branches (green). We next simulated the steady-state WNT9b concentration profile on the extracted kidney geometry, using the finite element method. We assumed uniform WNT9b production on the epithelium (Neumann boundary condition), as well as uniform Fickean diffusion and linear decay, both on the epithelium and in the mesenchyme (for details see Methods section). The kidney cortex, or the mesenchymal boundaries, are assumed not to constitute diffusion barriers [20]. To visualize the simulated WNT9b concentration gradient in the mesenchyme, we integrated over the simulated concentration along rays in normal direction from the UB surface and projected the result back to their origin, where we use a colourmap to display the relative WNT9b concentration (Fig. 1C). Thus, those parts of the ureteric bud that are marked in red are predicted to be adjacent to the mesenchyme where the WNT9b concentration is highest. We find that all RVs are positioned close to red regions of the ureteric epithelium (Fig. 1C); see the 3D visualisations for closer inspection (Supp. Files S1, S2, Supp. Movies S2). The simulated reaction-diffusion model (Methods) only has a single free parameter, the gradient length, λ, which needs to be in the range 20–50 µm to achieve substantial ligand upconcentration in the branch corners (Fig. 1D). Such a gradient length is well within the reported physiological range ($\lambda \in [5, 90]$ µm) [5, 11, 15, 39, 41–43]. For much longer or shorter gradients, the ligand concentrations are either nearly uniformly high or low, respectively.

The average WNT9b concentration in the PTA/RV is 2-fold higher than in the SIX2 population (Fig. 1E), and in all segmented RVs, the predicted ligand concentration is higher than the background level in the SIX2 population (Supp. Table S1). We note that the segmented LHX1 domains represent only a rough proxy for the part of the metanephric mesenchyme, where WNT9b induces RV, as they include also mature RVs that have expanded spatially since their first induction by WNT9b [25]. Consistent with this, we find the highest predicted WNT9b concentration in the smallest (i.e. latest) RV (Fig. 1F). We further

note that the model predicts an elevated WNT9b concentration also at internal branch points, where RVs are not observed (Fig. 1G). The absence of RVs in these regions can be accounted to a lack of SIX2-positive CM cells in the inner parts of the developing kidney (Fig. 1G, orange; Supp. Video S2). RVs therefore cannot form at these internal branch points, even though the local WNT9b concentration is increased.

Dynamic coordination of branching and RV positioning

Since RVs emerge dynamically as the epithelial tree emerges via branching morphogenesis, we sought to test the mechanism in time-lapse videos that allow to follow the coordination between UB branching morphogenesis and the positioning of PTA/RVs over time. Because the imaging of 3D organ cultures is still challenging [7, 13], we took advantage of a liquid-air interface culture system, in which the kidney adopts a flattened shape, allowing the branching process to be followed via live imaging of a 2D projection of the whole tissue. To this end, we cultured E12.0 kidney explants for 48 hours (Fig. 2A). As previously done for the 3D geometries, we segmented the outlines of the UB epithelium, cortex, and PTA/RVs, and solved the same reaction-diffusion equation for WNT9b on the growing 2D geometries (Fig. 2B, Supp. Video S3). Again, the location of the RVs coincide with the highest ligand concentration, even though the flattened geometry of the cultured explants differs from that in the embryo. In some cases, we predict elevated WNT9b concentrations before PTA/RVs can be detected based on their morphology. Different from before, we do not have a molecular marker of RV formation in our kidney cultures, limiting us to more mature forms. Consistent with WNT9b being considered the most upstream regulator of RV formation [3], we predict elevated concentrations before morphological changes can be detected. In some cases, we predict RV formation at places where no RV form. These can be accounted to 2D projection artefacts. Even though the cultured kidneys are rather flat, some branches still grow above or below each other, resulting in the false impression of a branch point in the 2D projections (Supp. Fig. S1).

To determine the accurate 3D branching architecture and PTA/RV positions of the time-lapse culture, we fixed the cultures after the experiment was completed and immunostained for LHX1. By careful inspection of the 3D image of the culture endpoint (Fig. 2C, the corner artefacts can be identified (Supp. Fig. S1, Supp. Files S2). The diffusion simulation solved on the 3D tissue geometry confirms that PTA/RVs are located at the points of highest ligand concentration (Fig. 2C, Supp. Table S2). As in the 3D embryonic kidney, the WNT9b concentration is predicted to be about 2-fold higher in the RVs (Fig. 2D).

We conclude that PTA/RVs emerge dynamically during branching morphogenesis in the branch corners where the simulations predict high WNT9b concentrations.

A local WNT9b source induces ectopic RV formation

According to our model, the increased WNT9b concentrations in the branch corners induce PTA/RVs. However, previous studies reported that *Six2-Cre*-driven expression of *Wnt9b* does not lead to ectopic RV induction, while *Six2-Cre*-driven expression of stabilised β-catenin (*Ctnnb1*) or addition of GSK inhibitors both do [16, 18, 28]. To analyse the impact of a local increase in the WNT9b concentration, we compared cultures in which 1) the WNT9b concentration was increased locally via WNT9b-soaked beads, 2) the WNT9b concentration was increased globally by adding recombinant WNT9b to the explant cultures, and 3) WNT signalling was increased globally by adding CHIR99021, a potent GSK inhibitor, to the explant cultures.

We first sought to check whether a local increase in the WNT9b concentration induces ectopic PTA/RVs in close proximity to the source in kidney explants. To this end, E11.5 kidney explants were co-cultured with control and WNT9b-soaked beads (Fig. 3A–C, Supp. Movie 5). To confirm PTA/RV and nephron progenitor positions, the culture endpoints were immunostained for LHX1 and SIX2 (Fig. 3D-F). RV formation could indeed be observed close to the WNT9b source (Fig. 3B,C,E,F). Additionally, in one example, the most proximal branches and the future ureter bent towards the WNT9b source during explant culture (Fig. 3C, Supp. Movie 5), possibly as a consequence of the attraction of GDNF-secreting CM towards the bead. GDNF-secreting CM close to the bead could also cause ectopic branching from the future ureter, which is associated with a developing nephron (Fig. 3C,E, Supp. Movie 5). Such ectopic branches are sometimes also observed in regular kidney cultures [40]. Taken together, these results support a role for WNT9b in determining the position of PTA/RVs.

While WNT9b-soaked beads induced PTA/RVs locally (Fig. 3D–F), uniform supplementation of kidney cultures with WNT9b did not induce uniform PTA/RV formation (data not shown). Uniform activation of WNT signalling by supplementing kidney cultures with CHIR99021, however, led to ectopic PTA/RVs. We supplemented kidney cultures with 5 µM or 10 µM CHIR99021, followed by immunostaining for LHX1 and SIX2 to mark PTA/RVs and the CM after 40h and 24h, respectively (Fig. 3G). While developing nephrons are located in UB corners in controls, uniformly supplied CHIR99021 induces ectopic RV formation. With a lower CHIR concentration, RVs appear below the cortex, regularly interspaced with SIX2-positive progenitors, whereas no LHX1 is detected close to the UB. A high CHIR concentration rapidly induces LHX1 in a large portion of the nephrogenic mesenchyme, which appears to be expanded relative to the UB. In both cases, branching morphogenesis is impaired as GDNF-secreting cap mesenchyme progenitors differentiate.

In summary, we confirm earlier reports that uniform WNT9b fails to induce ectopic RV, but we now show that a localised increase in WNT9b does result in ectopic RVs. We conclude that a local increase in the WNT9b concentration, as will result from the geometric effects proposed here, can instruct nephrogenesis to occur in branch corners (Fig. 3H).

Optimal branch kink angle and curvature

Finally, we wondered whether the kidney geometry was particularly suited to permit the coordination of branching morphogenesis and nephrogenesis via geometric effects. The ligand upconcentration can be expected to depend on two geometric properties: the branching angle, and the tissue curvature in the corner.

To investigate the impact of the branching angle, we simulated the steady-state reaction-diffusion equation (Methods) on a 2D domain with a 1D ligand source of constant length, L, kinked in the middle by an angle Θ (inset Fig. 4A). As expected, we find the ratio of the resulting concentration in the corner, c_1, to the concentration at the outer ends of the source, c_2, to monotonically increase with smaller Θ (Fig. 4A). The results are similar whether we use constant uniform production or a constant outflux from the source, and are independent of the relative gradient lengths λ/L. For the smallest tested angle, $\Theta = 10°$, we find a more than 30-fold higher concentration at the kink. However, for such a sharp kink, branches would grow into each other upon consecutive branching, resulting in rapid termination of branching. To permit continued branching, the

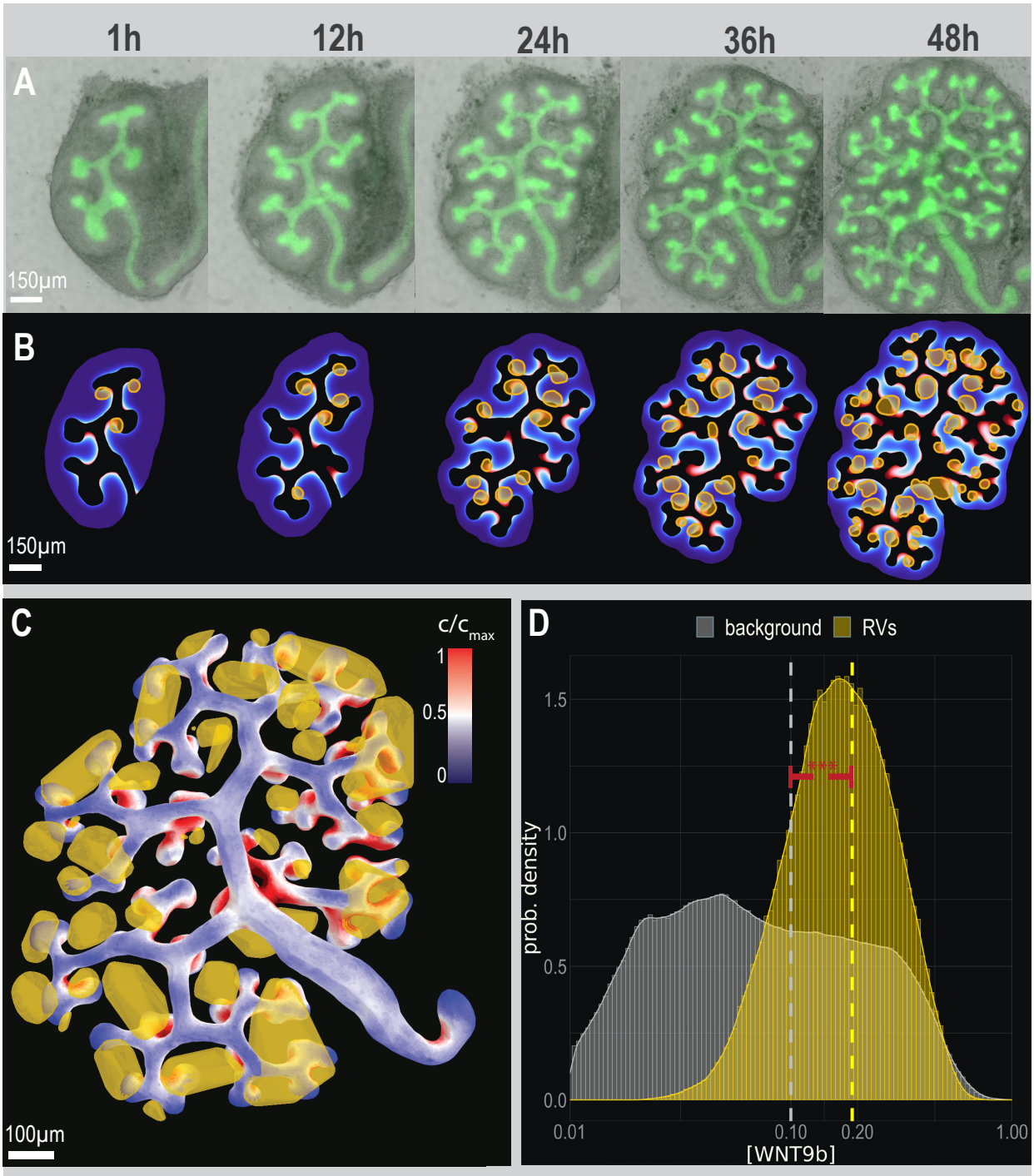

Figure 2: Dynamic coordination of branching and RV positioning. (A) Widefield live imaging of E12 HoxB7-Venus kidneys cultured for 48h; transgenic labeling of uteric bud (UB). (B) Dynamic simulations of uniform WNT9b secretion from the branching UB leads to highest ligand concentration (red) in the UB corner regions, preceding the emergence of RVs (yellow). (C) Simulation of WNT9b on the 3D geometry of the culture endpoint (48h). Uniform secretion of WNT9b from the UB leads to the highest ligand concentration (red) in the UB corner regions, coinciding with the positions of RVs (yellow). The plot shows the integrated concentration profile along the normal direction towards the mesenchyme projected back on the surface of the UB. (D) Concentration distribution inside and outside of RVs. Simulations are run on the geometry depicted in D. The simulated mean WNT9b concentration inside the RVs (yellow dashed line; $c/\bar{c}_{\mathrm{non-RV}} = 1.89 \pm 1.02$ (SD)) lies significantly above the predicted mean concentration in the mesenchyme (grey dashed line; $c/\bar{c}_{\mathrm{non-RV}} = 1.00 \pm 1.22$ (SD)); ($p < 0.001$, Welch's two-sample t-test, $t = 85.34$). All simulations were carried out with $\lambda = 30$ µm.

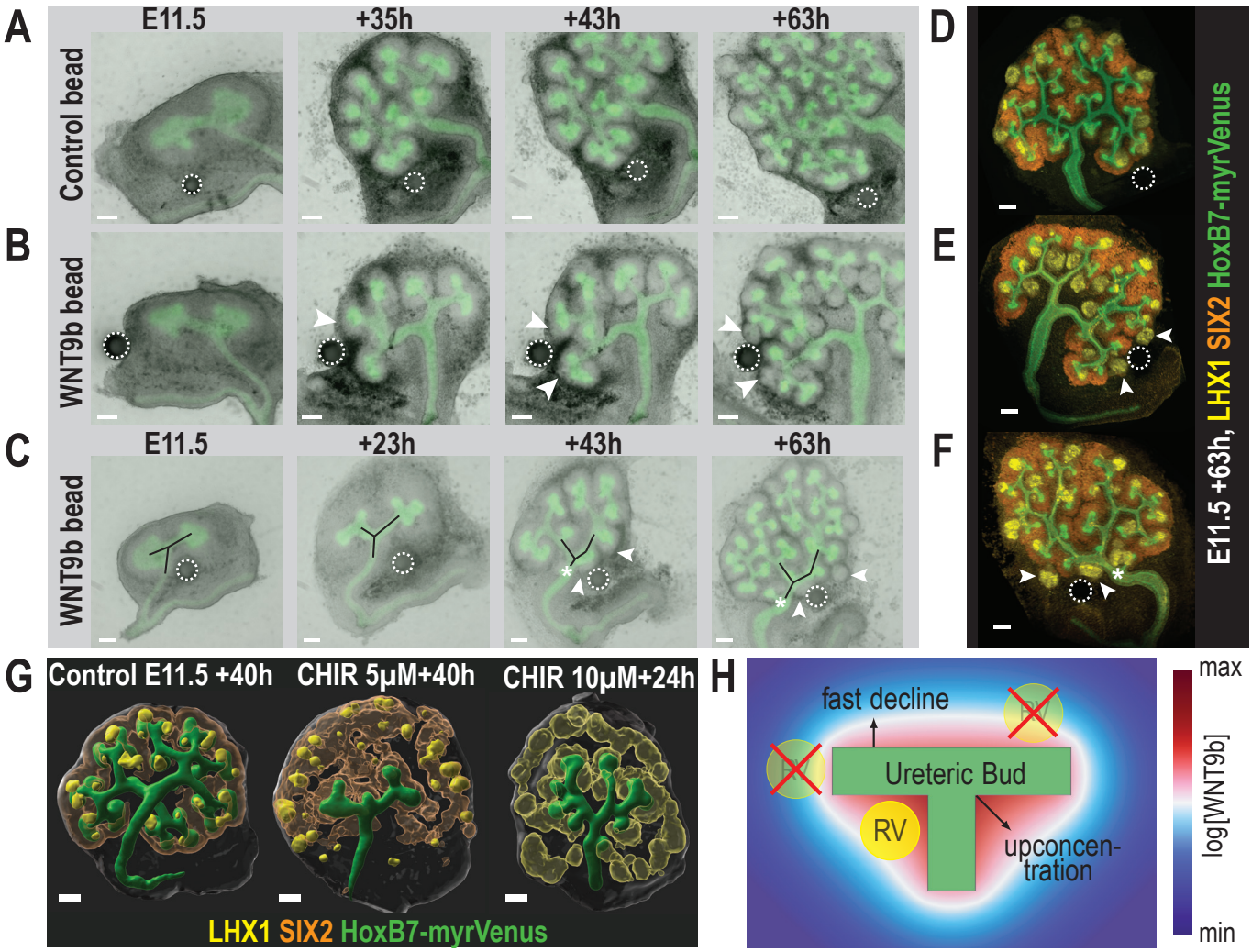

Figure 3: A local WNT9b source induces RV formation. HoxB7/myr-Venus kidney explants were cultured with control (A) or WNT9b-soaked (B, C) beads (dashed white circles). White arrowheads mark the position of renal vesicles that are forming in close proximity to the WNT9b source. (C) UB branches (black lines) bend toward the WNT9b source over time, potentially following CM cells that are attracted to the WNT9b-soaked bead. Ectopic branching from the future ureter (white asterisk). (D–F) 3D rendered LSFM data of the explant culture endpoints, immunostained for LHX1 and SIX2 for control (D) and WNT9b-soaked (E, F) beads. The white asterisk marks the same branch as in C. (G) 3D Imaris surfaces of HoxB7/myr-Venus kidney explants (segmented UB in green, outer surface transparent), immunostained for LHX1 and SIX2 (control and 5µM). Control; RVs form in the corners of UB branches; treated with 5µM CHIR99021 for 40h; LHX1+ clusters form away from the UB, interspersed with SIX2+ progenitors; treated with 10µM CHIR99021 for 24h; High uniform WNT activation results in *Lhx1* expression in most of the expanded metanephric mesenchyme. Scale bars 100 µm. (H) Diffusion simulation on a simplified UB branch, highlighting ligand upconcentration and RV positioning by geometric effects.

branching angle must exceed 90° on average. In the E12.5 kidney, we observe the angles between tip and parent branches to range from 81–121°, with a mean of $98.8 \pm 11.9°$ (SD) (Fig. 4B). This value is slightly lower than previously reported, possibly because previous analyses included internal angles, which increase during development as the ureteric tree remodels [34–36]. For the measured branching angles (Fig. 4B), we expect a 2-fold upconcentration of the ligand in the corner niches (Fig. 4A), as indeed observed in our E12.5 kidney simulations (Figs. 1E, 2D). We conclude that the branching angles in the kidney maximise the WNT9b concentration in the branch corners, while still permitting regular branching of most tips.

To investigate the impact of the branch curvature, we consider a bent 1D source (red line) of length L and curvature $\kappa = 1/R$, where R is the radius of the circular arc that the source follows (inset Fig. 4C). As the investigated geometric effects must be independent of the chosen length scale, we normalise all length scales with the source length, L. Accordingly, we consider a normalised gradient length, λ/L, a normalised curvature, $\kappa L/\pi$, and a normalised distance from the source, $x\pi/L$. Here, L/π is the radius of a semi-circle with circumference L. Moreover, we consider a normalised concentration that quantifies the relative difference between the concentration profile resulting from a curved ($c(\kappa, x)$) and straight ($c(0, x)$) source, normalised by the concentration at the straight source, $c(0, 0)$:

$$c_{\text{norm}}(\kappa, x) = \frac{c(\kappa, x) - c(0, x)}{c(0, 0)}.$$

We analyse the concentration profile along a straight line (blue) orthogonal to the center of the source (Fig. 4C, inset). Concave curvature ($x > 0$) results in ligand upconcentration, while convex curvature ($x < 0$) has the opposite effect and results in reduced concentrations (Fig. 4C). The normalised relative concentration profiles for maximal curvature ($\kappa = \pi/L$) peak at a similar relative distance from the source, $x \approx L/\pi$, with longer gradients (larger λ/L) peaking slightly closer to the

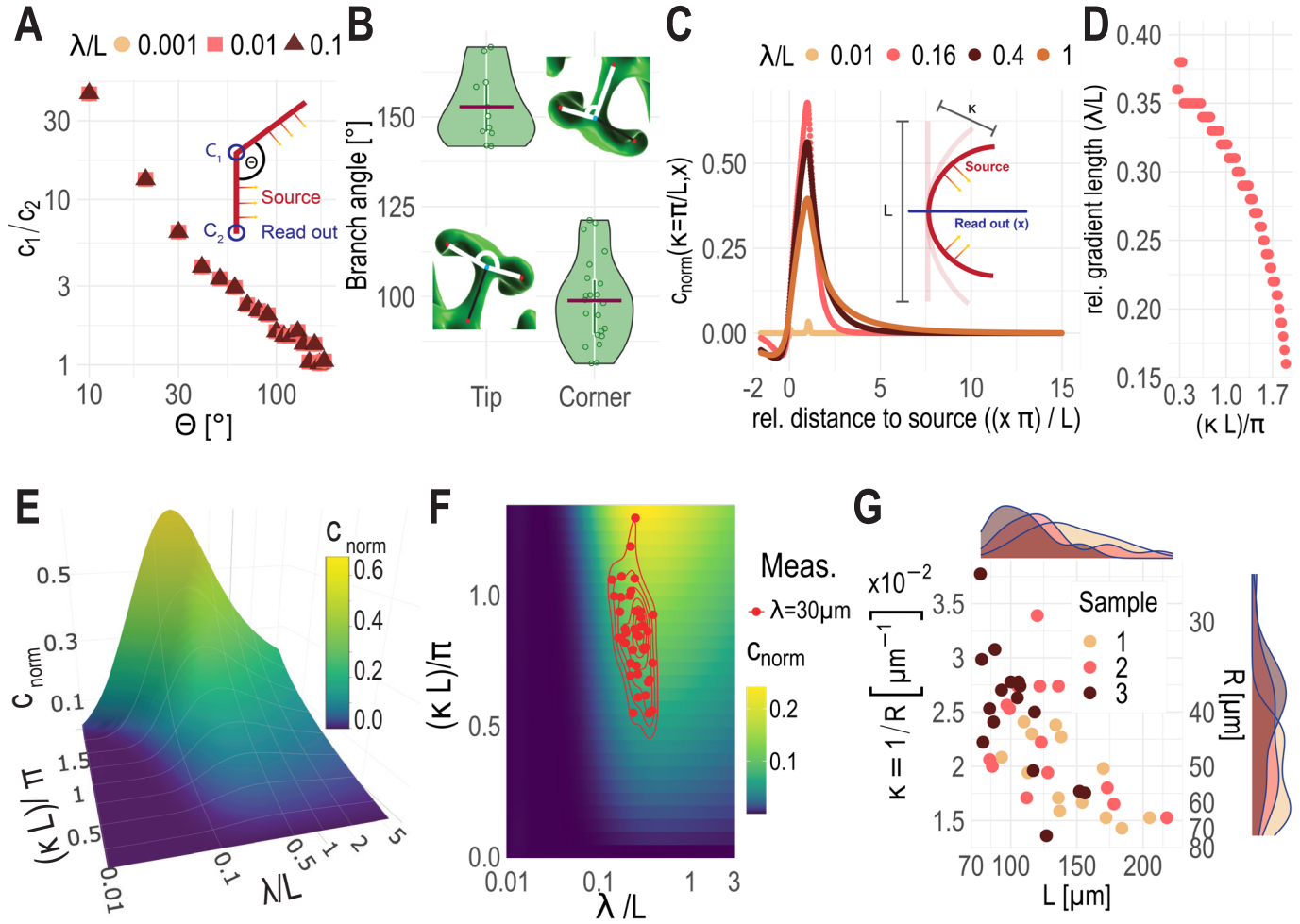

Figure 4: Optimal source kink angle and source curvature.(A) The concentration at the corner, c_1 is highest relative to the endpoint of the source, c_2, the smaller the angle, Θ, between the source parts. The same results are obtained with different relative gradient lengths, λ/L. The 2D simulations were carried out with constant flux boundary conditions at the source, but similar results are obtained with constant production in the source (inset, red). Note the logarithmic axes. (B) Measured branching angles in embryonic kidneys (E12.5). Measured were the outer angle (tip) and inner angle (corner). The insets describe the location of measurement. (C) The concentration profile originating from the center (inset, blue) of half-circular sources (inset, red) depend on the relative gradient length λ/L. The highest concentrations are observed in the concave part for $\lambda/L = 0.16$. (D) The highest ligand upconcentration depends on relative gradient length, λ/L and the curvature of the source, κ. The higher the curvature, the lower, the optimal gradient length for which maximal upconcentration is achieved. Displayed are the values with the highest concentration per simulated curvature, i.e. the ridge in panel E. (E) Relationship of relative gradient length, λ/L, curvature of the source, κ, and the relative concentration increase, c_{norm} at the readout position $x = L/\pi$. The concentration increases with curvature and peaks at $\lambda/L = 0.16$. (F) For $\lambda = 30$ µm, the measured branch lengths and curvatures in E12.5 kidneys (panel G) result in maximal upconcentration (red dots). (G) Measurements of curvature, radius, and length of ureter branch corners at positions where renal vesicles form. Analysis is based on three E12.5 kidneys.

source (Fig. 4C). The highest upconcentration is achieved for $\lambda/L = 0.16$. At smaller curvatures, the optimal relative gradient length increases (Fig. 4D), and the maximal upconcentration drops (Fig. 4E). Fig. 4D traces the ridge of the surface shown in Fig. 4E.

While the strongest upconcentration is achieved for the greatest curvature (Fig. 4E,F), high curvature implies small corner radii that may not leave sufficient room to accommodate PTA/RVs. The smallest PTA/RV that we detect in E12.5 kidneys have a diameter of about 25 µm, such that the curvature cannot exceed 0.08 µm^{-1}. The larger RV in E12.5 kidneys reach 100 µm in diameter along the UB, which bounds the curvature to about 0.02 µm^{-1} from below, if spherical RVs are to fill the niche without any gaps. We note that in later stages, RVs, however, depart from a spherical shape and develop into S-shaped bodies.

To determine the physiological branch length and corner curvature, we obtained three E12.5 kidneys and measured the curvature and length of each UB where a RV was detected (Fig. 4G). The curvature of the branch corners is between 0.014–0.038 µm^{-1} (Fig. 4G). We observe an anti-correlation between the branch length and branch curvature, suggesting that the curvature is highest in newly forming PTA. This is consistent with previous observations that showed that the expanding PTA/RV reduces the curvature of the ureteric epithelium [21].

For a given curvature, κ, and source length, L, there is an optimal gradient length, λ, that yields the highest upconcentration in the branch corner (Fig. 4E,F). For the measured branch curvatures ($\kappa = 0.0224 \pm 0.0056$ µm^{-1} (SD)) and lengths ($L = 123.65 \pm 35.08$ µm), we predict the highest ligand upcon-

centration for a gradient length of $\lambda = 30$ µm (Fig. 4F). This is consistent with our simulations on the 3D embryonic kidney geometries (Fig 1D, and such a gradient length is well within the reported range for morphogen gradients in other developmental systems, i.e. $\lambda \in [5, 90]$ µm [5, 11, 15, 39, 41–43].

We conclude that the geometry of the ureteric tree appears to be optimised to permit a substantial upconcentration of WNT9b at the branch corners over large enough distances to induce sizeable RVs, while permitting continued branching during development.

Conclusion

During kidney development, nephrogenesis and branching morphogenesis must be coordinated such that a single nephron connects to each ureteric branch point, thereby ensuring efficient drainage of the kidney. How this coordination is achieved has long remained elusive, even though the key molecular regulators, most notably WNT9b, have long been identified [3]. We have now shown that geometric effects lead to a higher WNT9b concentration in the branch corners of the ureteric tree, even though *Wnt9b* is expressed uniformly along the ureteric epithelium. As WNT9b induces PTA/RVs, these geometric effects can coordinate nephrogenesis with branching morphogenesis.

We show that the geometric effects are strongest, the smaller the branch angle, and the higher the branch curvature (Fig. 4A,C). The branch angle is indeed the smallest that it can be while permitting continued branching, and the corner curvature is the highest it can be while accommodating the PTA/RVs in the branch corners. This suggests that the geometry is optimised to permit strong ligand upconcentration in the branch corners. Finally, we show that the ligand upconcentration depends on the gradient length, which must be in a physiologically plausible range to ensure significant ligand upconcentration. While the WNT9b gradient length remains to be determined experimentally, we expect it to be at least 20 µm.

The role of tissue geometry for patterning has long been recognised [24, 26], and it will be interesting to see to what extent the here-identified patterning principle will apply to other developmental processes. The geometric concentration effect could be exploited also in tissue engineering applications [27] to generate non-uniform, localised morphogen distributions.

Methods

Ethical statement

Animal experiments were performed in accordance with Swiss federal law and the ordinance issued by the Canton Basel-Stadt and approved by the veterinary office of the Canton Basel-Stadt, Switzerland (approval number 2777/26711).

Mouse strains

Labeling of the ureteric bud was achieved by using the Hoxb7/myr-Venus transgenic allele [MGI: Tg(Hoxb7-Venus*)17Cos; [4]]. Timed pregnancies were set and checked daily for vaginal plugs to obtain the desired embryonic ages. Here, homozygous Hoxb7/myr-Venus males were crossed with RjOrl:SWISS wild-type females (higher pregnancy rates and larger litters).

Explant culture live imaging

Embryonic kidneys were dissected using fine forceps and tungsten needles in cold phosphate-buffered saline (PBS) and collected in a petri dish containing cold culture medium (DMEM-F12 supplemented with 10% fetal bovine serum, 1x GlutaMAX, 1x penicillin/streptomycin). The dissected kidneys were cultured at liquid-air interface on top of a porous filter membrane insert in a 6-well plate containing 1.5ml culture medium per well. To activate WNT signalling, the medium was supplemented with 5 or 10mM CHIR99021 (Stemcell technologies 72052), or with 200, 500, or 750ng/ml WNT9b (Peprotech 120-49) diluted in the culture medium. To locally deliver WNT9b, Affi-Gel Blue beads (Biorad 153-7302) were rinsed with PBS and incubated in 40µg/ml WNT9b (Peprotech 120-49) or in PBS (control) for 1 h at 37°C. Several beads were transferred into PBS to rinse off excess protein solution, one bead was selected using a P10 micro-pipette, and positioned close or on top of a kidney explant using fine forceps. The culture medium was changed every 48h.

Volumetric lightsheet microscopy and image analysis

Tissue clearing, immunofluorescence, and lightsheet fluorescence microscopy (LSFM) were performed as previously described (Susaki et al., 2015; Conrad et al., 2021). Blocking and antibody incubation was done using 3% bovine serum albumin (BSA) (Sigma-Aldrich A7906-10G) and 0.3% TritonX (Sigma-Aldrich T8787) in 1x PBS. Primary antibodies were incubated for 48h using the following dilutions: anti-LIM1/LHX1 (abcam ab229474) 1:200; anti-LIM1/LHX1 (antibody 4F2, deposited to the DSHB by Jessell, T.M. / Brenner-Morton, S. (DSHB Hybridoma Product 4F2)) 1:50; anti-SIX2 (proteintech 11562-1-AP) 1:200. All secondary antibodies were diluted 1:500 and incubated for 24h. The volumetric LSFM imaging data was imported into Imaris (Bitplane, Oxford Instruments) and 3D-rendered. To obtain segmentations of the ureteric bud, the renal vesicles, and the kidney cortex, Imaris surfaces were generated by intensity- and volume-based thresholding of the respective channels and manually corrected where needed (DAPI nuclear staining was imaged using a 405 nm laser, myr-Venus was imaged using a 488 nm laser, fluorophore-conjugated secondary antibodies were imaged using a 561 nm or a 647 nm laser). For the branching angle measurements, binary images were created in Imaris, skeletonised in 3D using the Fiji plugin "Skeletonize3D" and pruned over several iterations to remove wrongly segmented, small side branches. The cleaned tree was analysed using BoneJ2 to measure global angles at triple-junctions [9].

Computational model

We describe the spatio-temporal distribution of WNT9b, $c(\vec{x}, t)$, with a steady-state ($\partial c/\partial t = 0$) reaction-diffusion equation of the form

$$\lambda^2 \Delta c - c = 0, \tag{1}$$

where Δ is the Laplace operator. The equation has a single free parameter, λ, the gradient length, which is determined by the ratio of the diffusion coefficient and the turn-over rate. As the WNT gradient length has not yet been reported in mice, we set the gradient length to our estimated optimal $\lambda = 30$ µm (Figs. 1E, 4F), unless otherwise stated. As boundary condition on the surface of the ureter, we used a Neumann boundary condition of the form

$$-\vec{n} \cdot (\nabla c) = j \tag{2}$$

with the surface normal vector $\vec{n}$. As the absolute WNT9b concentration is not known, we only consider relative concentrations, $c/c_{\max}$, and j can be chosen freely without affecting our conclusions. The kidney cortex, or the mesenchyme boundaries are unlikely to constitute diffusion barriers in uncultured

kidneys [20], and we therefore solved the equations in a large enough box that the outer boundaries do not affect the solution.

We used the same simulation setup for the 3D and 2D kidney simulations. The 2D simulations differ only in that the reaction-diffusion equation is solved on a growing domain. As the cultured kidneys were imaged only every 60 minutes to avoid photo-toxicity, we interpolated the time points in between by computing displacement fields describing the morphological change from one captured culture time point to the next, using minimal distance mapping, as described earlier [31]. These vector fields are implemented in the simulation to prescribe a mesh deformation mimicking the observed growth process and allowing to predict WNT9b localisation on a continuous growing domain (Fig. S4) [12, 23].

All simulations were performed using the finite element method in COMSOL Multiphysics v6.0 (COMSOL AB, Stockholm, Sweden), as described before [12, 23].

References

[1] U. Blank, A. Brown, D. C. Adams, M. J. Karolak, and L. Oxburgh. BMP7 promotes proliferation of nephron progenitor cells via a JNK-dependent mechanism. *Development*, 136:3557–3566, 2009. doi: 10.1242/dev.036335.

[2] A. C. Brown, S. D. Muthukrishnan, J. A. Guay, D. C. Adams, D. A. Schafer, J. L. Fetting, and L. Oxburgh. Role for compartmentalization in nephron progenitor differentiation. *Proc. Natl. Acad. Sci. U.S.A.*, 110, 2013. doi: 10.1073/pnas.1213971110.

[3] T. J. Carroll, J. S. Park, S. Hayashi, A. Majumdar, and A. P. McMahon. Wnt9b plays a central role in the regulation of mesenchymal to epithelial transitions underlying organogenesis of the mammalian urogenital system. *Dev. Cell*, 9:283–292, 2005. doi: 10.1016/j.devcel.2005.05.016.

[4] X. Chi, A.-K. Hadjantonakis, Z. Wu, D. Hyink, and F. Costantini. A transgenic mouse that reveals cell shape and arrangement during ureteric bud branching. *Genesis*, 47:61–66, 2009. doi: 10.1002/dvg.20452.

[5] M. Cohen, A. Kicheva, A. Ribeiro, R. Blassberg, K. M. Page, C. P. Barnes, and J. Briscoe. Ptch1 and Gli regulate Shh signalling dynamics via multiple mechanisms. *Nat. Commun.*, 6:6709, 2015. doi: 10.1038/ncomms7709.

[6] A. N. Combes, J. G. Lefevre, S. Wilson, N. A. Hamilton, and M. H. Little. Cap mesenchyme cell swarming during kidney development is influenced by attraction, repulsion, and adhesion to the ureteric tip. *Dev. Biol.*, 418:297–306, 2016. doi: 10.1016/j.ydbio.2016.06.028.

[7] L. Conrad, S. V. M. Runser, H. Fernando Gómez, C. M. Lang, M. S. Dumond, A. Sapala, L. Schaumann, O. Michos, R. Vetter, and D. Iber. The biomechanical basis of biased epithelial tube elongation in lung and kidney development. *Development*, 148:dev194209, 2021. doi: 10.1242/dev.194209.

[8] F. Costantini and R. Kopan. Patterning a complex organ: branching morphogenesis and nephron segmentation in kidney development. *Dev. Cell*, 18:698–712, 2010. doi: 10.1016/j.devcel.2010.04.008.

[9] R. Domander, A. A. Felder, and M. Doube. BoneJ2 - refactoring established research software. *Wellcome Open Res.*, 6, 2021. doi: 10.12688/wellcomeopenres.16619.2.

[10] A. T. Dudley, R. E. Godin, and E. J. Robertson. Interaction between FGF and BMP signaling pathways regulates development of metanephric mesenchyme. *Genes Dev.*, 13: 1601–1613, 1999. doi: 10.1101/gad.13.12.1601.

[11] P. Fried, M. Sanchez-Aragon, D. Aguilar-Hidalgo, B. Lehtinen, F. Casares, and D. Iber. A Model of the Spatio-temporal Dynamics of Drosophila Eye Disc Development. *PLoS Comput. Biol.*, 12:e1005052, 2016. doi: 10.1371/journal.pcbi.1005052.

[12] P. Germann, D. Menshykau, S. Tanaka, and D. Iber. Simulating Organogenesis in COMSOL. In *COMSOL Conference 2011*, 2011. URL `https://www.comsol.com/paper/download/100817/iber_paper.pdf`.

[13] H. F. Gómez, M. S. Dumond, L. Hodel, R. Vetter, and D. Iber. 3D cell neighbour dynamics in growing pseudostratified epithelia. *eLife*, 10:e68135, 2021. doi: 10.7554/eLife.68135.

[14] N. Khoshdel Rad, N. Aghdami, and R. Moghadasali. Cellular and molecular mechanisms of kidney development: from the embryo to the kidney organoid. *Front. Cell Dev. Biol.*, 8:183, 2020. doi: 10.3389/fcell.2020.00183.

[15] A. Kicheva, P. Pantazis, T. Bollenbach, Y. Kalaidzidis, T. Bittig, F. Jülicher, and M. González-Gaitán. Kinetics of Morphogen Gradient Formation. *Science*, 315:521–525, 2007. doi: 10.1126/science.1135774.

[16] S. M. Kiefer, L. Robbins, and M. Rauchman. Conditional expression of wnt9b in six2-positive cells disrupts stomach and kidney function. *PLoS One*, 7:e43098, 2012.

[17] A. Kispert, S. Vainio, and A. P. McMahon. Wnt-4 is a mesenchymal signal for epithelial transformation of metanephric mesenchyme in the developing kidney. *Development*, 125:4225–4234, 1998. doi: 10.1242/dev.125.21.4225.

[18] S. Kuure, A. Popsueva, M. Jakobson, K. Sainio, and H. Sariola. Glycogen synthase kinase-3 inactivation and stabilization of beta-catenin induce nephron differentiation in isolated mouse and rat kidney mesenchymes. *J. Am. Soc. Nephrol.*, 18:1130–1139, 2007. doi: 10.1681/ASN.2006111206.

[19] K. T. Lawlor, L. Zappia, J. Lefevre, J.-S. Park, N. A. Hamilton, A. Oshlack, M. H. Little, and A. N. Combes. Nephron progenitor commitment is a stochastic process influenced by cell migration. *eLife*, 8:e41156, 2019. doi: 10.7554/eLife.41156.

[20] R. S. Levinson, E. Batourina, C. Choi, M. Vorontchikhina, J. Kitajewski, and C. L. Mendelsohn. Foxd1-dependent signals control cellularity in the renal capsule, a structure required for normal renal development. *Development*, 132: 529–539, 2005. doi: 10.1242/dev.01604.

[21] N. O. Lindström, G. D. S. Brandine, T. Tran, A. Ransick, G. Suh, J. Guo, A. D. Kim, R. K. Parvez, S. W. Ruffins, E. A. Rutledge, et al. Progressive recruitment of mesenchymal progenitors reveals a time-dependent process of cell fate acquisition in mouse and human nephrogenesis. *Dev. Cell*, 45:651–660, 2018. doi: 10.1016/j.devcel.2018.05.010.

[22] M. H. Little. Improving our resolution of kidney morphogenesis across time and space. *Curr. Opin. Genet. Dev.*, 32:135–143, 2015. doi: 10.1016/j.gde.2015.03.001.

[23] D. Menshykau and D. Iber. Simulating Organogenesis with COMSOL: Interacting and Deforming Domains. In *COMSOL Conference 2012*, 2012.

[24] D. Menshykau, P. Blanc, E. Unal, V. Sapin, and D. Iber. An interplay of geometry and signaling enables robust lung branching morphogenesis. *Development*, 141:4526–4536, 2014. doi: 10.1242/dev.116202.

[25] J. W. Mugford, J. Yu, A. Kobayashi, and A. P. McMahon. High-resolution gene expression analysis of the developing mouse kidney defines novel cellular compartments within the nephron progenitor population. *Dev. Biol.*, 333:312–323, 2009. doi: 10.1016/j.ydbio.2009.06.043.

[26] C. M. Nelson, M. M. VanDuijn, J. L. Inman, D. A. Fletcher, and M. J. Bissell. Tissue Geometry Determines Sites of Mammary Branching Morphogenesis in

Organotypic Cultures. *Science*, 314:298–300, 2006. doi: 10.1126/science.1131000.

[27] M. Nikolaev, O. Mitrofanova, N. Broguiere, S. Geraldo, D. Dutta, Y. Tabata, B. Elci, N. Brandenberg, I. Kolotuev, N. Gjorevski, et al. Homeostatic mini-intestines through scaffold-guided organoid morphogenesis. *Nature*, 585:574–578, 2020. doi: 10.1038/s41586-020-2724-8.

[28] J. S. Park, M. T. Valerius, and A. P. McMahon. Wnt/beta-catenin signaling regulates nephron induction during mouse kidney development. *Development*, 134:2533–2539, 2007. doi: 10.1242/dev.006155.

[29] J. S. Park, W. Ma, L. L. O'Brien, E. Chung, J. J. Guo, J. G. Cheng, M. T. Valerius, J. A. McMahon, W. H. Wong, and A. P. McMahon. Six2 and Wnt regulate self-renewal and commitment of nephron progenitors through shared gene regulatory networks. *Dev. Cell*, 23:637–651, 2012. doi: 10.1016/j.devcel.2012.07.008.

[30] A. O. Perantoni, O. Timofeeva, F. Naillat, C. Richman, S. Pajni-Underwood, C. Wilson, S. Vainio, L. F. Dove, and M. Lewandoski. Inactivation of FGF8 in early mesoderm reveals an essential role in kidney development. *Development*, 132:3859–3871, 2005. doi: 10.1242/dev.01945.

[31] C. A. Schwaninger, D. Menshykau, and D. Iber. Simulating organogenesis: Algorithms for the image-based determination of displacement fields. *ACM Trans. Model. Comput. Simul.*, 25, 2015. doi: 10.1145/2688908.

[32] M. Self, O. V. Lagutin, B. Bowling, J. Hendrix, Y. Cai, G. R. Dressler, and G. Oliver. Six2 is required for suppression of nephrogenesis and progenitor renewal in the developing kidney. *EMBO J.*, 25:5214–5228, 2006. doi: 10.1038/sj.emboj.7601381.

[33] A. Sharma, M. Meer, A. Dapkunas, A. Ihermann-Hella, S. Kuure, S. Vainio, D. Iber, and F. Naillat. FGF8 induces chemokinesis and regulates condensation of mouse nephron progenitor cells. *bioRxiv*, 2022. doi: 10.1101/2022.02.07.478973.

[34] K. Short, M. Hodson, and I. Smyth. Spatial mapping and quantification of developmental branching morphogenesis. *Development*, 140:471–478, 2013. doi: 10.1242/dev.088500.

[35] K. M. Short, A. N. Combes, J. Lefevre, A. L. Ju, K. M. Georgas, T. Lamberton, O. Cairncross, B. A. Rumballe, A. P. McMahon, N. A. Hamilton, et al. Global quantification of tissue dynamics in the developing mouse kidney. *Dev. Cell*, 29:188–202, 2014. doi: 10.1016/j.devcel.2014.02.017.

[36] S. Sims-Lucas, C. Argyropoulos, K. Kish, K. McHugh, J. F. Bertram, R. Quigley, and C. M. Bates. Three-dimensional imaging reveals ureteric and mesenchymal defects in Fgfr2-mutant kidneys. *J. Am. Soc. Nephrol.*, 20:2525–2533, 2009. doi: 10.1681/ASN.2009050532.

[37] K. Stark, S. Vainio, G. Vassileva, and A. P. McMahon. Epithelial transformation of metanephric mesenchyme in the developing kidney regulated by Wnt-4. *Nature*, 372:679, 1994. doi: 10.1038/372679a0.

[38] M. Tomita, M. Asada, N. Asada, J. Nakamura, A. Oguchi, A. Y. Higashi, S. Endo, E. Robertson, T. Kimura, T. Kita, A. N. Economides, J. Kreidberg, and M. Yanagita. Bmp7 maintains undifferentiated kidney progenitor population and determines nephron numbers at birth. *PLoS One*, 8:e73554, 2013. doi: 10.1371/journal.pone.0073554.

[39] O. Wartlick, P. Mumcu, A. Kicheva, T. Bittig, C. Seum, F. Jülicher, and M. González-Gaitán. Dynamics of Dpp signaling and proliferation control. *Science*, 331:1154–1159, 2011. doi: 10.1126/science.1200037.

[40] T. Watanabe and F. Costantini. Real-time analysis of ureteric bud branching morphogenesis in vitro. *Dev. Biol.*, 271:98–108, 2004. doi: 10.1016/j.ydbio.2004.03.025.

[41] S. R. Yu, M. Burkhardt, M. Nowak, J. Ries, Z. Petrasek, S. Scholpp, P. Schwille, and M. Brand. Fgf8 morphogen gradient forms by a source-sink mechanism with freely diffusing molecules. *Nature*, 461:533–636, 2009. doi: 10.1038/nature08391.

[42] M. Zagorski, Y. Tabata, N. Brandenberg, M. P. Lutolf, G. Tkačik, T. Bollenbach, J. Briscoe, and A. Kicheva. Decoding of position in the developing neural tube from antiparallel morphogen gradients. *Science*, 356:1379–1383, 2017. doi: 10.1126/science.aam5887.

[43] S. Zhou, W.-C. Lo, J. L. Suhalim, M. A. Digman, E. Gratton, Q. Nie, and A. D. Lander. Free Extracellular Diffusion Creates the Dpp Morphogen Gradient of the Drosophila Wing Disc. *Curr. Biol.*, 22:668–675, 2012. doi: 10.1016/j.cub.2012.02.065.

Code Availability

The source code and COMSOL model files are released under the 3-clause BSD license and are available as a public git repository at `https://git.bsse.ethz.ch/iber/Publications/2022_mederacke_conrad_renal_vesicles`.

Acknowledgements

This work was funded by the Swiss National Science Foundation under Sinergia grant no. CRSII5_170930. We thank Marco Meer for interesting discussions.

Competing Interests

None declared.

Author Contributions

Experiments: L.C., M.M.; Image processing: M.M., L.C.; Simulations: M.M.; Theory and modelling: D.I., R.V., M.M.; Writing: D.I., M.M., L.C., R.V.; Visualisation: M.M., L.C., R.V.; Supervision: R.V., D.I.; Conceptualisation: D.I.; Project administration: D.I.; Funding acquisition: D.I.

Supplementary Material

Supplementary Data

Table S1: Predicted concentration in the RV of an E12.5 kidney. Simulated normalized mean concentration, $c_{RV}/\bar{c}_{SIX2}$, inside each segmented RV and standard deviation. From the E12.5 Kidney used for Fig. 1D.

RV	norm. mean conc.	SD
RV1	2.10460123167059	0.784301184498161
RV2	1.72093520735421	0.462866825453608
RV3	2.28654758432875	0.816871034942931
RV4	1.98017417670302	0.83720111501182
RV5	2.23117441526323	0.689618259265129
RV6	2.3568583628366	0.523467432081343
RV7	1.98283250798053	0.82473092806899
RV8	1.84812853602427	0.953668436073596
RV9	1.57182549499172	0.872044894290876
RV10	1.9628332678972	0.75035306715877
RV11	2.39424794830583	0.549865863560481
RV12	1.93922717479229	0.738153807556894
RV13	2.1449830693159	0.800876969300404
RV14	2.20504185023655	0.767819761191748

Table S2: Predicted concentration in the RV at the endpoint of a 48h E12 kidney organ culture. Simulated normalized mean concentration, $c_{\mathrm{RV}}/\bar{c}_{\mathrm{non-RV}}$, inside each segmented RV and standard deviation. Data is used for Fig.2C.

RV	norm. mean conc.	SD
RV2	2.10602869143368	0.865891759736307
RV3	2.39633179034101	1.02155989048948
RV4	2.1794033928943	0.491551394783072
RV5	2.50354585477477	0.949306209541453
RV6	1.19875236328727	0.400841699812111
RV7	3.20621665375077	0.927622218020915
RV8	2.16330452422214	0.26907137945461
RV9	1.45149991887175	0.955669046703233
RV10	1.1603377502205	0.634118097480708
RV11	1.18313561605536	0.56973814274605
RV12	1.9770055010327	0.422359947881685
RV13	2.61087897640778	1.27221908830602
RV14	2.30820398752971	0.726921896400643
RV15	1.74221195946699	0.551859535288539
RV16	1.38554784276591	0.56939462145328
RV17	1.21861688074208	0.570333627267588
RV18	1.47981018823209	0.313881437792843
RV19	1.87876667878206	0.66599472828535
RV20	2.11994315439893	NA
RV21	2.12939258048643	0.405640546007605
RV22	4.23105274820811	0.542938083604097
RV23	2.44503808420562	0.37771344027245
RV24	1.57248837358867	0.0664712192381408
RV25	0.870694550696065	0.213030682298554
RV26	3.34617857249682	0.90849935263358
RV27	1.57566404358719	0.595511339627565
RV28	1.15036709541044	0.802842631621146
RV29	2.49444861802165	NA
RV30	2.1378005391086	0.314617161620359
RV31	2.3707929051979	0.880875866705377
RV32	1.3370858137239	0.280760394180415
RV33	1.31627602898568	0.566726093992604
RV34	0.949754890153809	0.331289394146189
RV35	1.857382730673	0.976338342187977
RV36	1.47186283926757	0.472160970205341
RV37	1.49904163271374	0.690861912731939
RV38	2.08935987231969	0.867268667227173
RV40	2.889296635084	1.01471087864029
RV41	1.72510195292669	0.715175478306938
RV42	2.09127267858737	0.788542947345446
RV43	3.1680435626253	0.873187094370571
RV44	2.56916313378432	1.11354165143339
RV45	2.40888900393421	0.812114682445789

Supplementary Figures

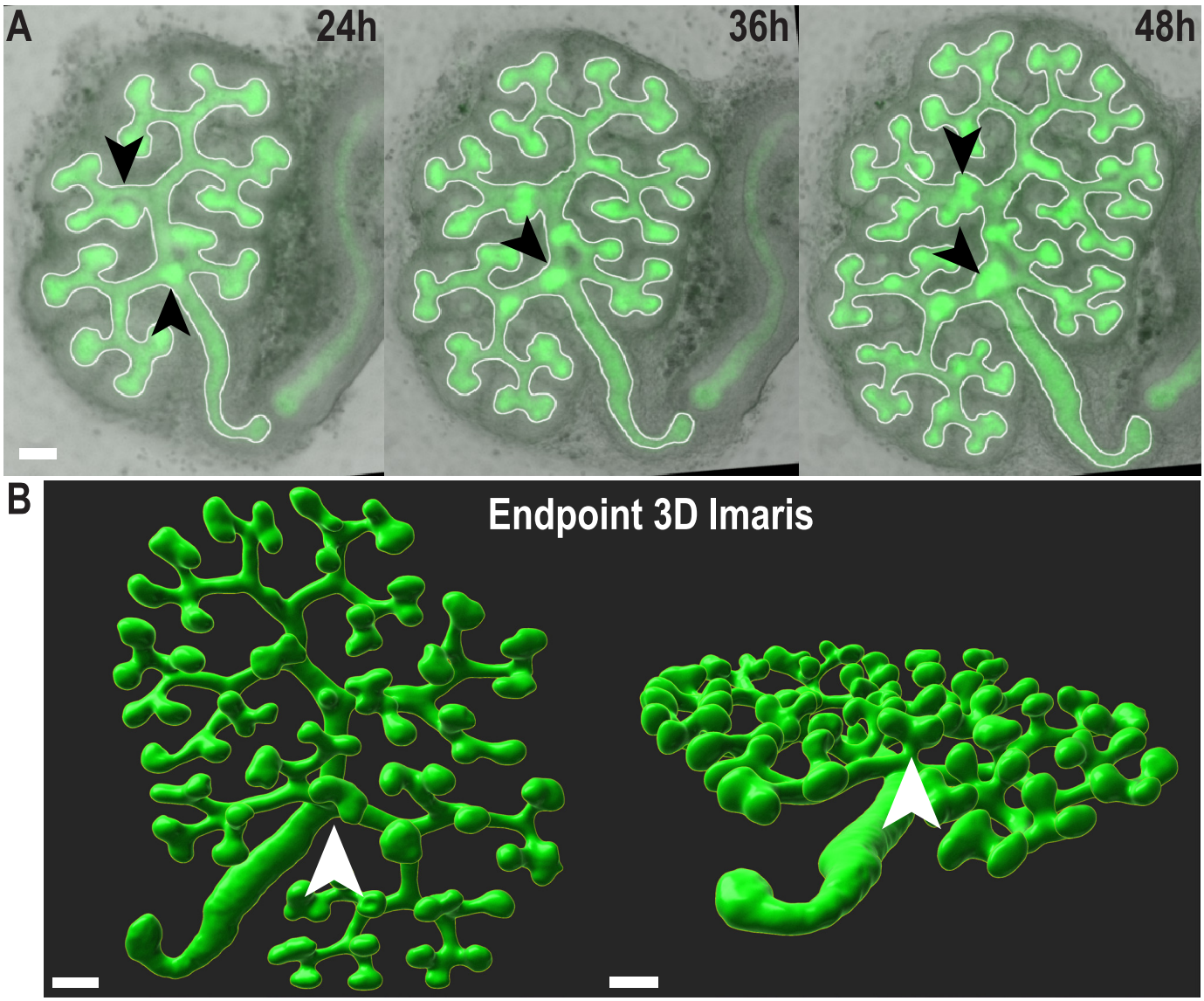

Figure S1: 2D segmentation can result in false impression of branch points. (A) Widefield kidney (E12) live imaging; transgenic labeling of the ureteric bud (UB) in green, overlayed with the 2D segmentation of the UB used in dynamic simulations (white outline) (Fig. 2B). Black arrowheads mark points of undersegmented branches due to the 3D geometry of the tissue. (B) 3D rendered light-sheet data of the UB at the culture endpoint. White arrowheads highlight UB branches that grow below the ureter and are therefore not visible in the 2D segmentation. Scale bars 100µm.

Supplementary Movies

Movie S1:

3D geometry of an E12.5 metanephric kidney. Movie of 3D lightsheet microscopy of an E12.5 kidney and subsequent surface segmentation, which are the basis for downstream analysis. Green is the UB, labelled by HoxB7/myr-Venus expression, orange is SIX2. LHX1, the RV marker is depicted in yellow.

Movie S2:

3D diffusion simulation on realistic kidney geometry. 3D diffusion simulation based on image-segmented surfaces. Red areas have high, white medium, and blue low simulated WNT9b concentration. Orange are SIX2-positive cells, yellow are identified RVs. Grey is the kidney cortex. First the simulation is shown in 3D, then it slices through the volume.

Movie S3:

2D kidney explant culture shows the sequential formation of RVs E12.5 mouse kidneys were cultured for 48h. One frame corresponds to 1h in culture. These images are the basis for the shapes used for the 2D diffusion simulations. Frames were used for Figure 2A.

Movie S4:

Temporal coordination of nephrogenesis and UB branching. 2D diffusion simulations on segmented live imaging data of kidney explant cultures. Red areas have high, white medium, and blue low simulated WNT9b concentration. Imaging time points where captured once per hour. The growth in-between time points is reconstructed by computing vector fields describing the change in geometry and doing simulations on a continuous growing domain.

Movie S5:

Explant cultures with local WNT9b source. Time-lapse movies of E11.5 kidneys cultured for 63h. Left: Kidney co-cultured with a control PBS-soaked bead; Middle and right: Kidneys co-cultured with WNT9b-soaked beads. HoxB7/myr-Venus expression is shown in green, brightfield in grey.

Supplementary Files

HTML S1:

3D diffusion simulation on realistic kidney geometry - interactive plot. Interactive 3D plot of the simulated WNT9b concentration projected on the UB surface of a E12.5 mouse kidney. Red areas have high, white medium, and blue low simulated WNT9b concentration. Yellow surfaces are RVs.

HTML S2:

3D simulation on cultured kidney geometry. Interactive 3D plot of the simulated WNT9b concentration projected on the UB surface of a explant culture endpoint after 48h. Red areas have high, white medium, and blue low simulated WNT9b concentration. Yellow surfaces are RVs.

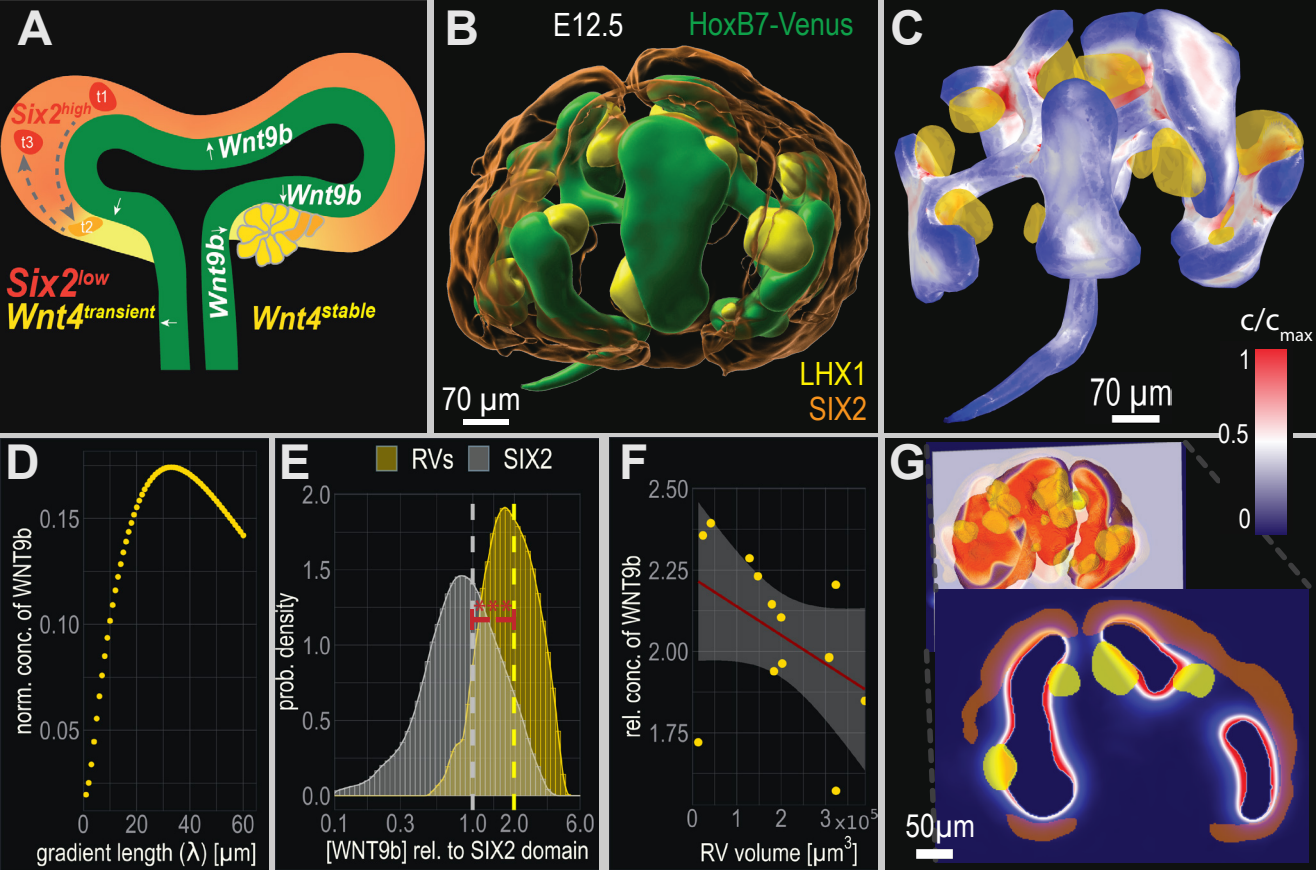
A
Six2high
t1
t3
t2
Wnt9b
Wnt9b
Wnt9b
Six2low
Wnt4transient
Wnt4stable
B
E12.5
HoxB7-Venus
LHX1
SIX2
70 µm
C
c/cmax
1
0.5
0
70 µm
D
norm. conc. of WNT9b
0.15
0.10
0.05
0
20
40
60
gradient length (λ) [µm]
E
RVs
SIX2
prob. density
2.0
1.5
1.0
0.5
0.0
0.1
0.3
1.0
2.0
6.0
[WNT9b] rel. to SIX2 domain
F
rel. conc. of WNT9b
2.50
2.25
2.00
1.75
0
1
2
3
x10^5
RV volume [µm^3]
G
50µm

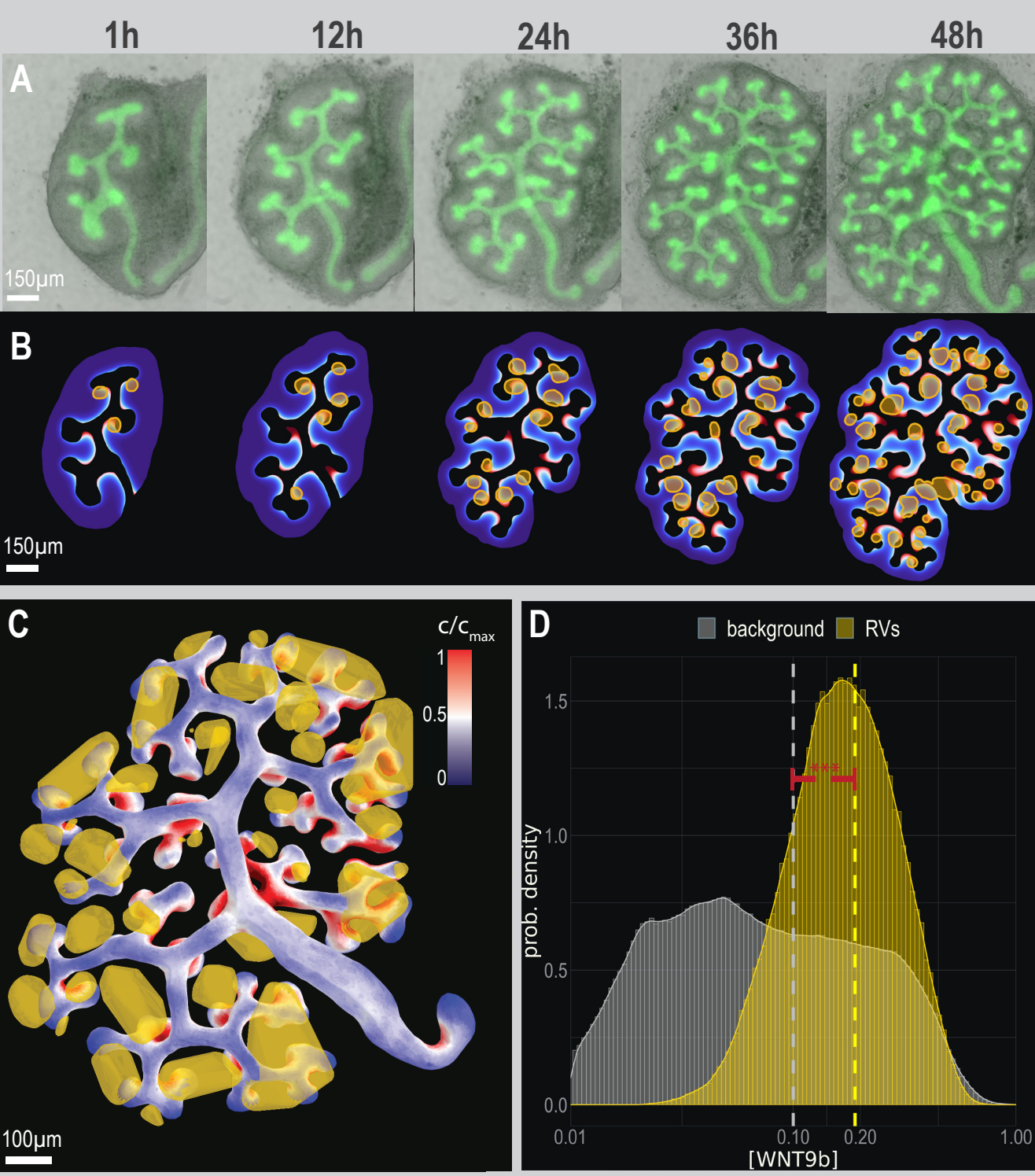
1h
12h
24h
36h
48h
A
150µm
B
150µm
C
c/c_max
1
0.5
0
100µm
D
background
RVs
prob. density
1.5
1.0
0.5
0.0
0.01
0.10
0.20
1.00
[WNT9b]

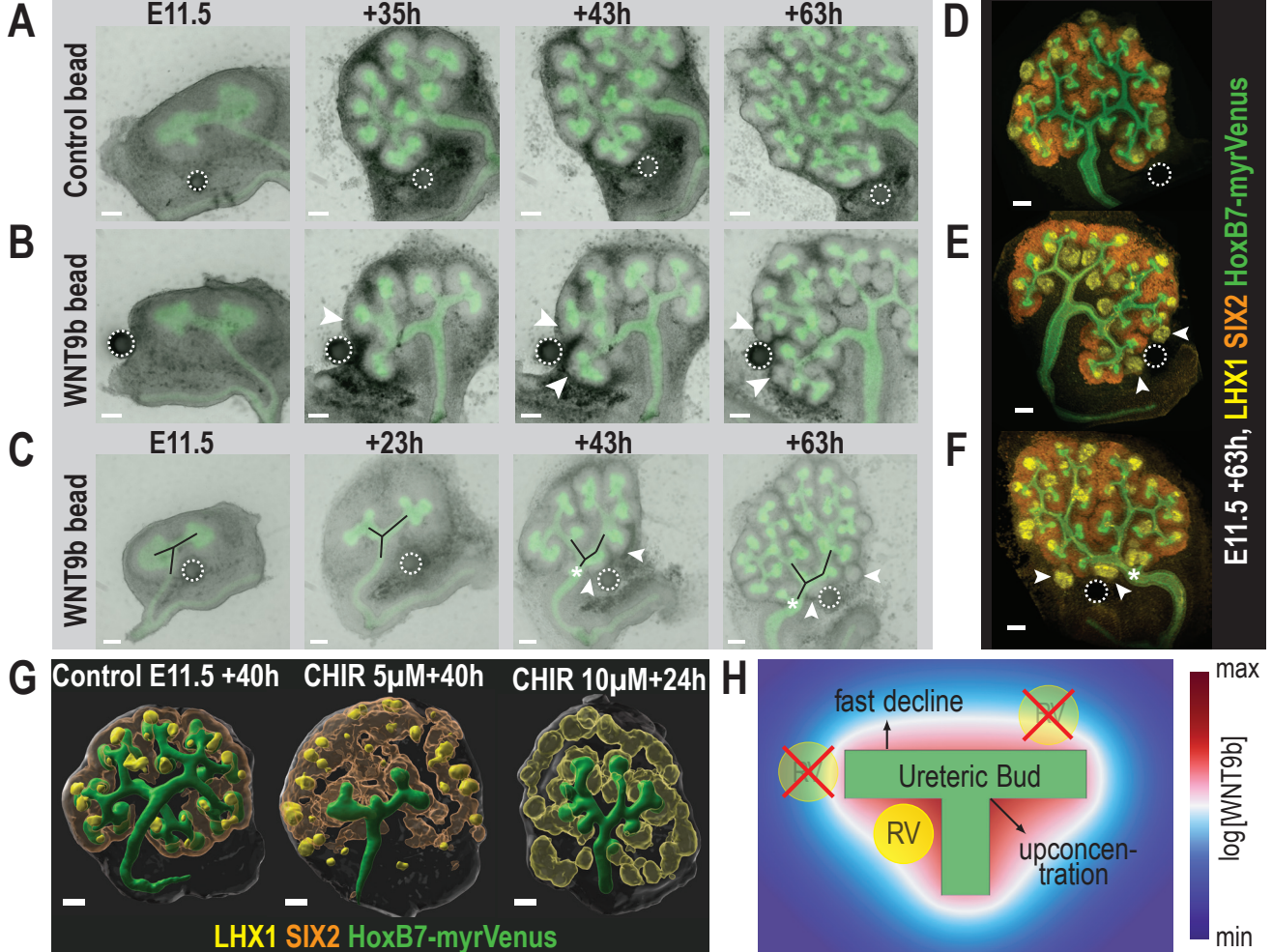
A
E11.5
+35h
+43h
+63h
Control bead
B
WNT9b bead
C
E11.5
+23h
+43h
+63h
WNT9b bead
D
E
F
E11.5 +63h, LHX1 SIX2 HoxB7-myrVenus
G
Control E11.5 +40h
CHIR 5μM+40h
CHIR 10μM+24h
LHX1 SIX2 HoxB7-myrVenus
H
fast decline
Ureteric Bud
RV
upconcen-
tration
max
log[WNT9b]
min

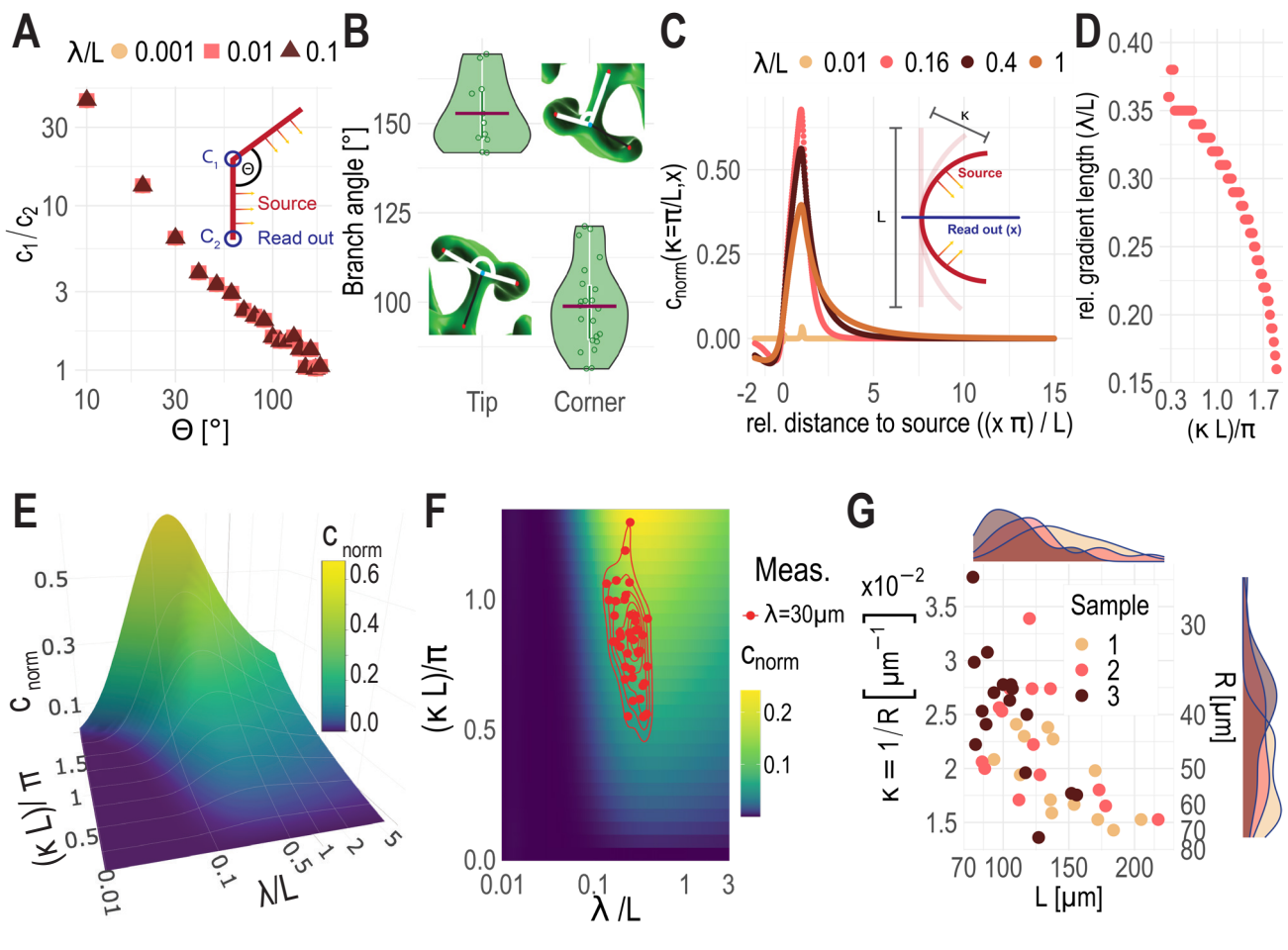
A
λ/L 0.001 0.01 0.1
c1/c2
Θ [°]
C1
C2
Source
Read out
B
Branch angle [°]
Tip
Corner
C
λ/L 0.01 0.16 0.4 1
cnorm(κ=π/L,x)
rel. distance to source ((x π) / L)
κ
L
Source
Read out (x)
D
rel. gradient length (λ/L)
(κ L)/π
E
cnorm
(κ L)/ π
λ/L
F
Meas.
λ=30µm
cnorm
(κ L)/π
λ /L
G
x10−2
κ = 1/R [µm−1]
L [µm]
R [µm]
Sample
1
2
3

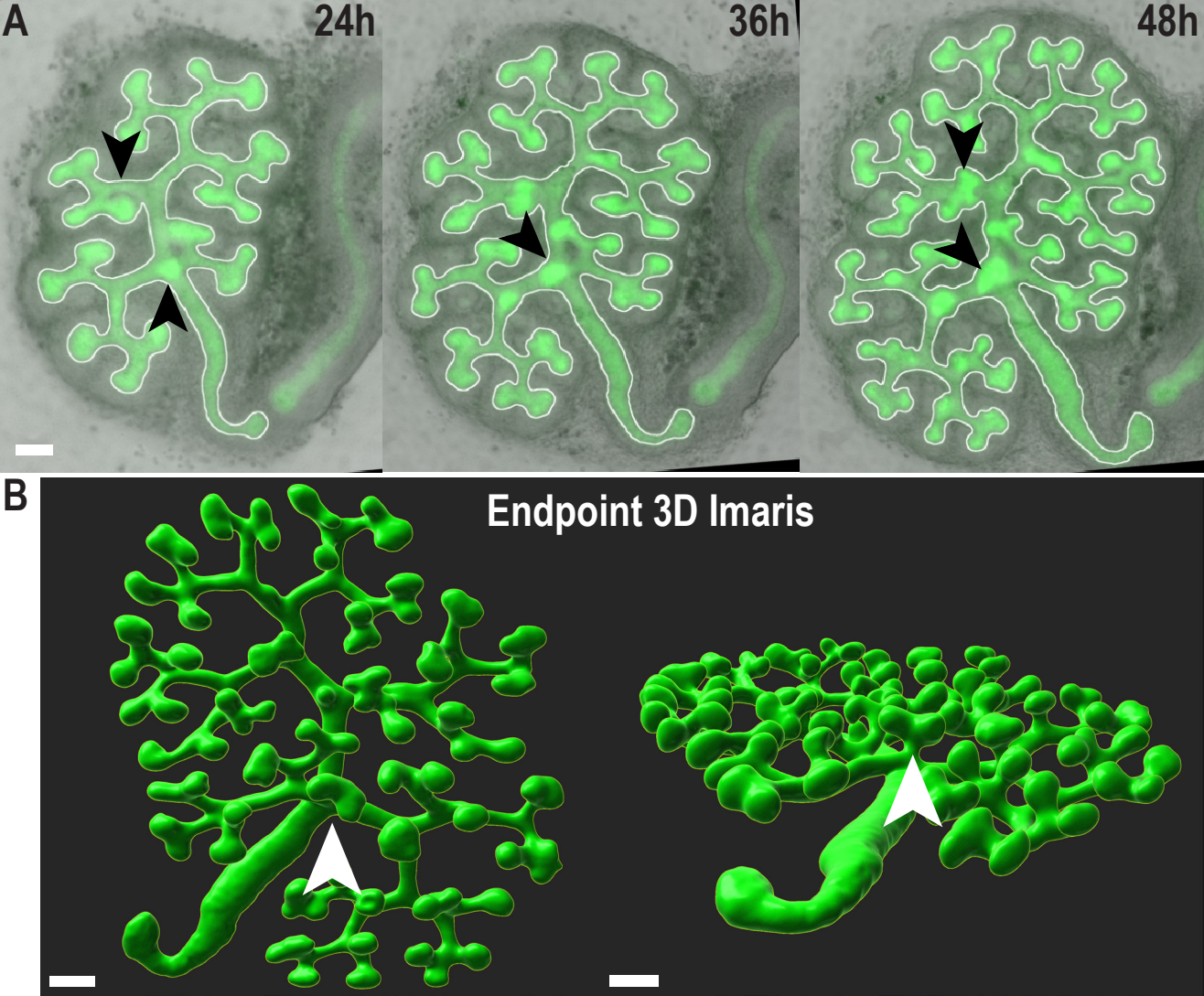
A
24h
36h
48h
B
Endpoint 3D Imaris